Supplementary Information

SUPPLEMENTARY FIGURES

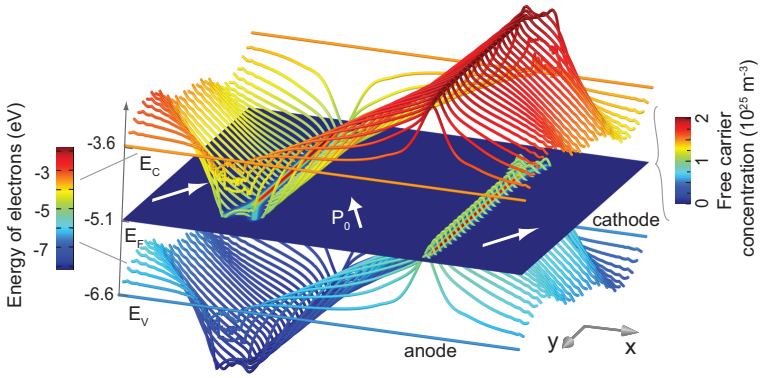

Supplementary Figure S1: **Two-dimensional potential profile.** Band bending in the vicinity of head-to-head and tail-to-tail sCDW, and electrodes with identical work function as $BaTiO_3$. Polarization divergence at head-to-head sCDW induces band banding into an extent when the bottom of the conduction band, E_C, drops bellow the Fermi level E_F, allowing the presence of screening free electrons. Top of the valence band, E_V, rises over the Fermi level at tail-to-tail sCDW, screening polarization charge by holes. Electrodes (anode and cathode) dictate flat potential profile which results in formation of transient regions between sCDW and electrodes. These regions are exposed to high built-in electric fields which nucleate wedge domains at junctions between head-to-head sCDW and anode and tail-to-tail sCDW and cathode. Dielectric gaps are created at the remaining two types of junctions. Note that this simulation is valid for ideal defect-free material.

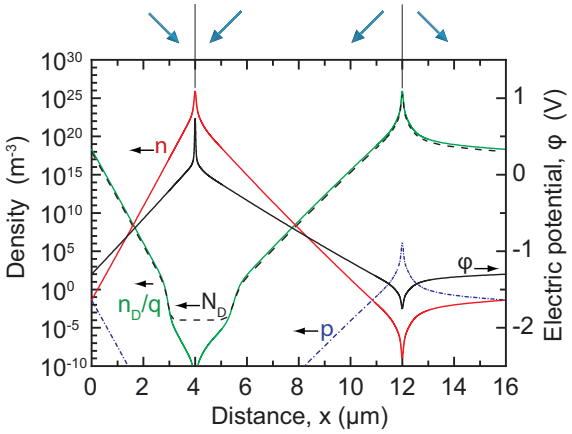

Supplementary Figure S2: **Potential profile and charge-carrier and defect densities.** 1-D phase field simulation of charge carrier and defect densities (left axis) and electric potential φ (right axis) across the head-to-head and tail-to-tail domain walls. Compensation of polarization charge at head-to-head wall requires accumulation of electrons, n, and depletion of oxygen vacancies N_D. The negligible remaining density of vacancies is not ionized which lowers the charge carrier density, n_D/q. The head-to-head wall accumulates holes p and almost fully ionized oxygen vacancies N_D. The electric potential φ forms a zig-zag profile across the domain walls. The oxygen vacancies almost fully replace screening holes at the tail-to-tail domain wall after $\sim 10^1$ hours with initial defect concentration $N_D|_{t=0} = 10^{18}$ m^{-3}. It makes the tail-to-tail walls significantly less conductive.

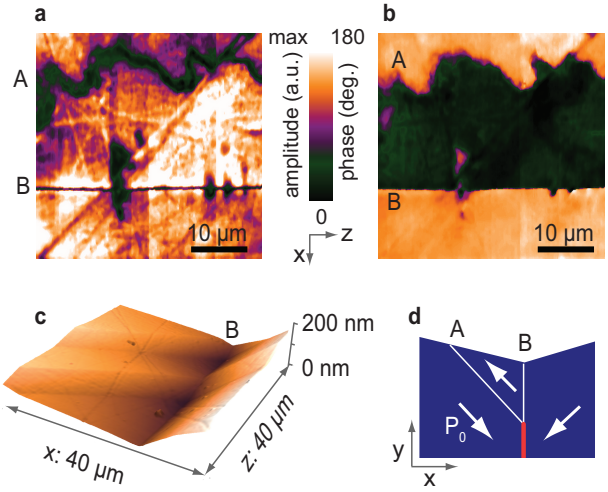

Supplementary Figure S3: **Scanning probe micrographs.** The atomic force (AFM) and piezo-response (PFM) scans of $[110]_c$ sample surface near a head-to-head sCDW were taken after removing the Pt electrodes. PFM amplitude, (**a**), and phase, (**b**), together with change of slope at AFM topography, (**c**), suggest that the straight boundary B is 90° ferroelectric/ferroelastic domain wall while the curved boundary A is 180° domain wall as illustrated in (**d**).

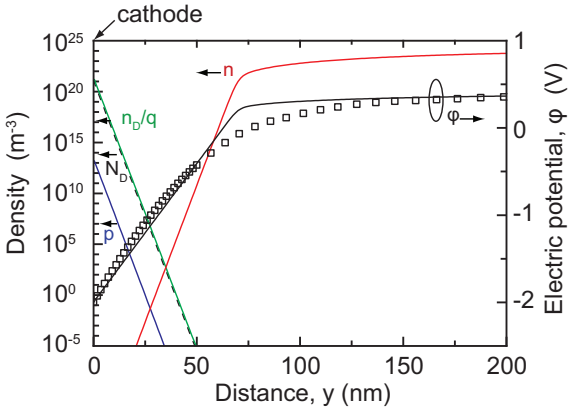

Supplementary Figure S4: **Charge/defect densities by the cathode.** 1-D phase field simulation of charge and defect densities (left axis) and electric potential along the head-to-head domain wall in the vicinity of the cathode. The electron concentration n almost fully screens the polarization charge at the wall. The presence of the Pt electrode causes a drop of the electron concentration n and potential φ in the region 100 nm bellow the anode. This region, on the other hand, accumulates oxygen vacancies N_D which carry charge n_D/q and holes p.

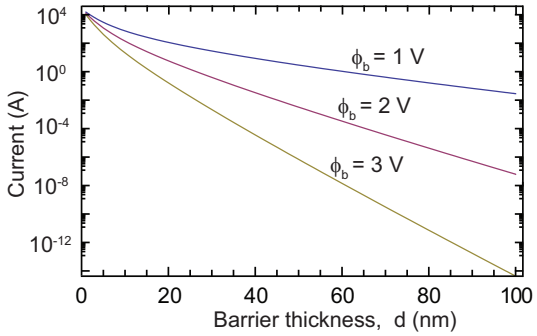

Supplementary Figure S5: **Tunneling current.** Dependence of tunneling current on barrier thickness for barrier heights $\phi_b = 1, 2, 3$ V. Voltage V=100 V.

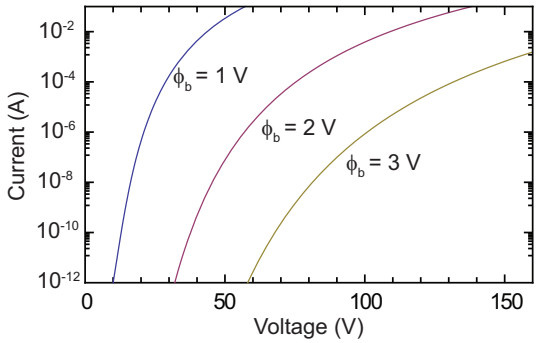

Supplementary Figure S6: **Tunneling current.** Tunneling current against voltage for barrier heights $\phi_{\rm b} = 1, 2, 3$ V when the barrier thickness is d=50 nm.

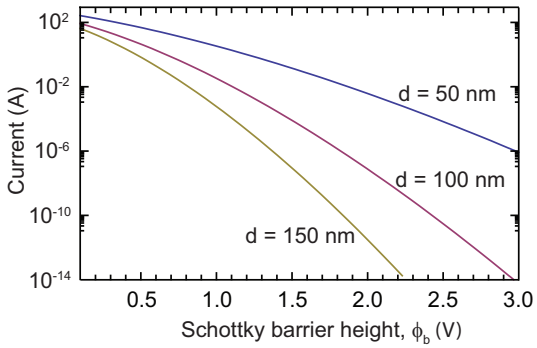

Supplementary Figure S7: **Tunneling current.** Tunneling current against barrier height for thicknesses $d = 50, 100, 150$ nm. Voltage V=100 V.

SUPPLEMENTARY TABLES

Parameter	Value	Unit	Ref.
α_1	$(T-381)3.34\times10^5$	Jm/C^2	
α_{11}	$(T-393)4.69\times10^6-2.02\times10^8$	Jm^5/C^4	
α_{12}	3.23×10^8	Jm^5/C^4	[36]
α_{111}	$(393-T)5.52\times10^7+2.76\times10^9$	Jm^9/C^6	
α_{112}	4.47×10^9	Jm^9/C^6	
α_{123}	4.91×10^9	Jm^9/C^6	
c_{11}	27.5×10^{10}	J/m^3	
c_{12}	17.9×10^{10}	J/m^3	[36]
c_{44}	5.43×10^{10}	J/m^3	
q_{11}	14.2×10^9	Jm/C^2	
q_{12}	-0.74×10^9	Jm/C^2	[36]
q_{44}	6.28×10^9	Jm/C^2	
G_{11}	51×10^{-11}	Jm^3/C^2	
G_{12}	-2×10^{-11}	Jm^3/C^2	[36]
G_{44}	2×10^{-11}	Jm^3/C^2	
Γ	4×10^4	$C^2/(Jms)$	[36]
ε_B	7.35	1	[36]
μ_n, μ_p	0.01	$cm^2/(Vs)$	[40]
β	1×10^{-8}	$cm^2/(Vs)$	$\star$
τ	100	ps	[41]
E_{C}	-3.6	eV	
E_{V}	-6.6	eV	
E_{D}	-4.0	eV	[33]
E_{F}	-3.98	eV	
	-5.1 (ideally defect-free case)	eV	
N	1×10^{24}	m^{-3}	[33]
$N_{\mathrm{D}}\vert_{t=0}$	1×10^{18}	m^{-3}	$\star$
	0 (ideally defect-free case)	m^{-3}	
z	2	1	
g	2	1	[33]

$\star$ Values of Vö mobility β and concentration $N_{\mathrm{D}}|_{t=0}$ of undoped $BaTiO_3$vary in literature by many orders of magnitude. We choose higher estimate of β from [38, 42, 43] for 400 K, which is counterbalanced with very low estimate of $N_{\mathrm{D}}|_{t=0}$ compared to Refs. [22, 33].

Supplementary Table S1: Values of material coefficients for $BaTiO_3$ used in the simulations.

SUPPLEMENTARY NOTES

Supplementary Note 1: The phase-field model

The phase-field simulation incorporates coupling between ferroelectric and wide-bandgap semiconductor properties including mobile defects. Model equations are obtained by Lagrange principle from Helmholtz free energy density [35]:

$$f[\{P_i, P_{i,j}, e_{ij}, D_i\}] = f^{(e)}_{\text{bulk}} + f_{\text{ela}} + f_{\text{es}} + f_{\text{grad}} + f_{\text{ele}}, \tag{S1}$$

where P_i is the ferroelectric part of polarization, $P_{i,j}$ its derivatives (the subscript ' $_{,i}$' represents the operator of spatial derivatives $\partial/\partial x_i$), D_i the electric displacement and $e_{ij} = 1/2(u_{i,j} + u_{j,i})$ is the elastic strain where u_i is a displacement vector.

The bulk free energy density

$$\begin{aligned} f^{(e)}_{\text{bulk}}[\{P_i\}] = & \\ & \alpha_1 \sum_i P_i^2 + \alpha^{(e)}_{11} \sum_i P_i^4 + \alpha^{(e)}_{12} \sum_{i>j} P_i^2 P_j^2 + \alpha_{111} \sum_i P_i^6 \\ & + \alpha_{112} \sum_{i>j} (P_i^4 P_j^2 + P_j^4 P_i^2) + \alpha_{123} \prod_i P_i^2 \end{aligned} \tag{S2}$$

is expressed for a zero strain as a six-order polynomial expansion [36], where $\alpha_i, \alpha^{(e)}_{ij}, \alpha_{ijk}$ are parameters fitted to the single crystal properties (Supplementary Table **S1**). The remaining contributions represent bilinear forms of densities of elastic energy $f_{\text{ela}}[\{e_{ij}\}] = 1/2 c_{ijkl} e_{ij} e_{kl}$, where c_{ijkl} is the elastic stiffness, electrostriction energy $f_{\text{es}}[\{P_i, e_{ij}\}] = -q_{ijkl} e_{ij} P_k P_l$, where q_{ijkl} are the electrostriction coefficients, gradient energy $f_{\text{wall}}[\{P_{i,j}\}] = 1/2 G_{ijkl} P_{i,j} P_{k,l}$, where G_{ijkl} are the gradient energy coefficients, and electrostatic energy $f_{\text{ele}}[\{P_i, D_i\}] = 1/(2\varepsilon_0 \varepsilon_B)(D_i - P_i)^2$, where ε_0 and ε_B are permittivity of vacuum and relative background permittivity, respectively. The zero-strain coefficients $\alpha^{(e)}_{ij}$ can be expressed in terms of usually introduced stress-free coefficients α_{ij} as follows:

$$\begin{aligned} \alpha^{(e)}_{11} &= \alpha_{11} + \frac{1}{6}\left(\frac{2(q_{11} - q_{12})^2}{c_{11} - c_{12}} + \frac{(q_{11} + 2q_{12})^2}{c_{11} + 2c_{12}} \right), \\ \alpha^{(e)}_{12} &= \alpha_{12} + \frac{1}{6}\left(\frac{2(q_{11} + 2q_{12})^2}{c_{11} + 2c_{12}} - \frac{2(q_{11} - q_{12})^2}{c_{11} - c_{12}} + \frac{3q_{44}^2}{4c_{44}} \right). \end{aligned}$$

By using the Legendre transformation to electric enthalpy

$$h[\{P_i, P_{i,j}, u_{i,j}, \varphi_{,i}\}] = f[\{P_i, P_{i,j}, e_{ij}, D_i\}] - D_i E_i,$$

where $E_i = -\varphi_{,i}$ is the electric field and φ the electric potential, and using Lagrange principle, we can uniformly express the set of field equations which govern the kinetics of ferroelectrics:

$$\left(\frac{\partial h}{\partial e_{ij}} \right)_{,j} = 0, \tag{S3}$$

$$\left(\frac{\partial h}{\partial E_i} \right)_{,i} = q(p - n) + n_{\text{D}}, \tag{S4}$$

$$\frac{1}{\Gamma} \frac{\partial P_i}{\partial t} - \left(\frac{\partial h}{\partial P_{i,j}} \right)_{,j} = -\frac{\partial h}{\partial P_i}. \tag{S5}$$

Equation (S3) defines the mechanical equilibrium while inertia is neglected. Equation (S4) represents Gauss's law of a dielectric including a nonzero concentration of free electrons n, holes p, and charge density of ionized donors n_{D}. Equation (S5) is the time dependent Landau-Ginzburg-Devonshire equation [37] which governs the spatiotemporal evolution of spontaneous polarization with kinetics given by coefficient Γ.

Coupling between the ferroelectric/ferroelastic system with its semiconductor properties is introduced by considering a nonzero density of free carriers (electron-hole) in the electrostatic equation (S4). The distribution of free carriers is governed by continuity equations:

$$q \frac{\partial n}{\partial t} + J^{(n)}_{i,i} = qR_n, \tag{S6}$$

$$q \frac{\partial p}{\partial t} + J^{(p)}_{i,i} = qR_p, \tag{S7}$$

where electron and hole currents $J_i^{(n)}$ and $J_i^{(p)}$, respectively, are governed by drift and diffusion as follows: $J_i^{(n)} = \mu_n(qnE_i + k_BTn_{,i})$ and $J_i^{(p)} = \mu_p(qpE_i - k_BTp_{,i})$. Here μ_n and μ_p are electron and hole mobilities, respectively. In the first step of calculation we analyze only the stationary solution in thermal equilibrium. In this step we can introduce the computationally convenient form of recombination rates R_n and R_p as follows: $R_n = -(n - n_0)/\tau$ and $R_p = -(p - p_0)/\tau$, where τ is life-time constant and n_0 and p_0 are electron and hole concentrations in thermal equilibrium:

$$\begin{aligned} n_0 &= NF_{1/2}\left(-\frac{E_\mathrm{C} - E_\mathrm{F} - q\varphi}{k_\mathrm{B}T}\right), \\ p_0 &= NF_{1/2}\left(-\frac{E_\mathrm{F} - E_\mathrm{V} + q\varphi}{k_\mathrm{B}T}\right). \end{aligned}$$

Here $F_{1/2}$ is the Fermi-Dirac integral. Density of states is given by the effective mass approximation:

$$N \simeq 2\left(\frac{m_\mathrm{eff}k_\mathrm{B}T}{2\pi\hbar^2}\right)^{\frac{3}{2}},$$

where effective mass $m_\mathrm{eff} = cm_e$ is assumed equal for electrons and holes. Results presented in the graphs correspond to $c = 0.117$, i.e. $N = 10^{24}$ m^{-3} [33].

The charge density of ionized donors is obtained as $n_\mathrm{D} = qzf(\varphi)N_\mathrm{D}$, where z is the donor valency,

$$f(\varphi) = 1 - \left(1 + \frac{1}{g}\exp\left(\frac{E_\mathrm{D} - E_\mathrm{F} - q\varphi}{k_\mathrm{B}T}\right)\right)^{-1}$$

is the fraction of ionized donors with the donor level E_D and the ground state degeneracy of the donor impurity level g [33].

The donor density N_D evolves through diffusion,

$$\frac{\partial N_\mathrm{D}}{\partial t} - \nabla\cdot\left(\beta N_\mathrm{D}\nabla\left(\frac{\partial W_\mathrm{D}}{\partial N_\mathrm{D}} + qzf(\varphi)\varphi\right)\right) = 0, \tag{S8}$$

where β is the donor mobility [38], and W_D is the contribution to the free energy due to defects which is assumed to be the usual free energy of mixing at small concentrations [39]. Values of the simulation parameter are introduced in Tab. **S1**.

The two-dimensional simulations (Fig. 4, Supplementary Fig. **S1** and squares in Supplementary Fig. **S4**) were performed with zero defect concentration $N_\mathrm{D} = 0$, on a simulation domain of 20×6 μm^2 (Fig. 4 and Supplementary Fig. **S4**) and 6×6 μm^2 (Supplementary Fig. **S1**). The numerical solution of equations (S3)-(S7) on the defined subdomain was performed by a finite element method with linear triangular elements of size 4 nm in the vicinity of domain walls and 40 nm inside domains. The boundary conditions are set to potential $\varphi = \Delta\phi = 0$ in Fig. 4 and Supplementary Fig. **S1**, and $\varphi = \Delta\phi = -0.8$ V in Supplementary Fig. **S4**, zero free-carrier flux, zero stress, and zero polarization gradient. Periodic boundary conditions in x-direction were applied in case of simulation shown in Supplementary Fig. **S1**. The simulations start from initial conditions that are defined as zero for all variables except polarization which is $P = \sqrt{2}(1,-1)P_0$ for $x < 0$ and $P = \sqrt{2}(-1,-1)P_0$ for $x > 0$, $P_0 = 0.262$ C/m^2 in the reference frame of Fig. 4. The initial condition in case of Supplementary Fig. **S1** is $P = \sqrt{2}(1,-1)P_0$ for $|x| > 1.5$ μm and $P = \sqrt{2}(-1,-1)P_0$ for $|x| < 1.5$ μm. The simulations reach thermal equilibrium in < 5 ns and gives solutions for the spatial distribution of polarization P_i, mechanical displacement u_i, electric potential φ, and concentrations of electrons n and holes p.

The calculation with applied voltage uses the thermal equilibrium as an initial condition and continues with recombination given by $R_n = R_p = -np/(\tau(n + p)) + G$ where $G = 10^{20}$ s^{-1} is a small free carrier generation. The boundary potential is applied as $\varphi = Vy/6 \times 10^{-6}$ V.

The one-dimensional calculation involves also equation (S8) which gives drift and ionization of donors and excludes the elasticity equation (S3) by putting $q_{ij} = 0$, $\alpha_{11}^{(e)} = \alpha_{11}$ and $\alpha_{12}^{(e)} = \alpha_{12}$. Since the defect drift is orders of magnitude slower than the polarization changes, the simulation is split into two steps. First, the distribution of polarization P_1, potential φ, and free carrier densities n, p are calculated and, second, the polarization is frozen and drift of donors N_D is calculated. The thermal equilibrium is reached after 10^5 s. The result of this simulation is shown in Supplementary Fig. **S2**.

The one-dimensional calculation along the domain wall (Supplementary Fig. **S4**) uses the polarization charge distribution extracted from two-dimensional simulation and continues with calculation of potential φ, free carrier densities n, p, and donor density N_{D}. The results are shown in Supplementary Fig. **S4** for head-to-head wall in the vicinity of the cathode.

Supplementary Note 2: Electron tunneling

To estimate the tunneling current we assumed the triangular potential barrier and the Wentzel - Kramers - Brillouin approximation of the transmission probability for the Fowler-Nordheim tunneling. Tunneling current is calculated as [44]

$$J_{\mathrm{t}} = A\frac{4\pi m_e q}{h^3}\int_{E_{\min}}^{E_{\max}} T_{\mathrm{C}}(\mathcal{E})S_{\mathrm{f}}(\mathcal{E})d\mathcal{E}, \tag{S9}$$

where A is the effective area of the tunneling (assumed 100 nm $\times$ 200 μm), $E_{\min}$ is the bottom of the conduction band in metal, $E_{\max}$ is the top of the potential barrier and h is the Plank constant. The supply function $S_{\mathrm{f}}(E)$ is for Fermi-Dirac distribution calculated as

$$S_{\mathrm{f}}(\mathcal{E}) = k_{\mathrm{B}}T\ln\frac{1+\exp\left(-\frac{\mathcal{E}-E_{\mathrm{F1}}}{k_{\mathrm{B}}T}\right)}{1+\exp\left(-\frac{\mathcal{E}-E_{\mathrm{F2}}}{k_{\mathrm{B}}T}\right)}$$

where E_{F1} is the Fermi level position in the metal when the external voltage is applied and E_{F2} is the Fermi level at the head-to-head sCDW. The transmission probability for the Wentzel-Kramers-Brillouin approximation is

$$T_{\mathrm{C}}(\mathcal{E}) = \exp\left(-4\frac{\sqrt{2m_e}d}{3\hbar qV}(q\Delta\phi-\mathcal{E})^{3/2}\right)$$

where d is the barrier thickness.

The tunneling current equation (S9) is calculated numerically and the results summarized in Supplementary Figs. **S5**-**S7**. The Fowler-Nordheim tunneling (without assistance of defects) exceeds the measured currents for barrier thickness $d \sim 90$ nm, and barrier height $\phi_{\mathrm{b}} \sim 2V$.

SUPPLEMENTARY REFERENCES

[35] Li, Y. L. and Chen, L. Q. Temperature-strain phase diagram for $BaTiO_3$thin films. *Appl. Phys. Lett.* **88**, 072905 (2006).

[36] Hlinka, J., Ondrejkovic, P., and Marton, P. The piezoelectric response of nanotwinned $BaTiO_3$. *Nanotechnology* **20**, 105709 (2009).

[37] Semenovskaya, S. and Khachaturyan, A. G. Development of ferroelectric mixed states in a random field of static defects. *J. Appl. Phys.* **83**, 5125–5136 (1998).

[38] Yoo, H. I., Chang, M. W., Oh, T. S., Lee, C. E., and Becker, K. D. Electrocoloration and oxygen vacancy mobility of $BaTiO_3$. *J. Appl. Phys.* **102**, 093701 (2007).

[39] Porter, D. and Easterling, K. *Phase Transformations in Metals and Alloys, Second Edition.* Taylor & Francis, (1992).

[40] Yoo, H. I., Song, C. R., and Lee, D. K. Electronic carrier mobilities of $BaTiO_3$. *J. Eur. Ceram. Soc.* **24**, 1259–1263 (2004).

[41] Smirl, A. L., et al. Picosecond photorefractive effect in $BaTiO_3$. *Opt. Lett.* **12**, 501–503 (1987).

[42] Benguigu.L. Electrical phenomena in barium-titanate ceramics. *J. Phys. Chem. Solids* **34**, 573–581 (1973).

[43] El Kamel, F., Gonon, P., Ortega, L., Jomni, F., and Yangui, B. Space charge limited transient currents and oxygen vacancy mobility in amorphous $BaTiO_3$thin films. *J. Appl. Phys.* **99**, 094107 (2006).

[44] Duke, C. *Tunneling in solids.* Academic Press, (1969).